Central Star Formation in Early-type Galaxy I Zw 81 in the Bootes Void

Divya Pandey[1] ⬤, Kanak Saha[2] ⬤, Ananta C. Pradhan[1] ⬤, and Sugata Kaviraj[3]
[1] Department of Physics and Astronomy, National Institute of Technology, Rourkela, Odisha 769 008, India; divya_pandey@nitrkl.ac.in
[2] Inter-University Centre for Astronomy & Astrophysics, Postbag 4, Ganeshkhind, Pune 411 007, India
[3] Centre for Astrophysics Research, Department of Physics, Astronomy and Mathematics, University of Hertfordshire, Hatfield AL10 9AB, UK

Abstract

The origin of star formation in customarily passively evolving early-type massive galaxies is poorly understood. We present a case study of a massive galaxy, I Zw 81, inside the Bootes void. The void galaxy is known to host active galactic nuclei (AGN). Our detailed 2D decomposition of the surface brightness distribution in the Canada France Hawaii Telescope (CFHT) g and r bands revealed multiple structural components such as a nuclear point source, a bar, a ring, and an inner exponential disk followed by an outer low surface brightness disk. I Zw 81 turns out to be a disk-dominated galaxy with lenticular morphology. The modeling of the multiwavelength spectral energy distribution shows that the galaxy is star-forming (SF), and belongs to the blue cloud. We find that the optical $(g-r)$ color of the bar is bluer than the disks, and the far- and near-ultraviolet emission inside the galaxy observed with Imaging Telescope onboard AstroSat is concentrated in the central few kpc region enclosing the bar. The strong bar might be playing a pivotal role in driving the gas inflow and causing SF activity in tandem with the minor merger-like interactions as evident from the deep CFHT data. The low-luminosity AGN is insufficient to quench the central SF. The results are peculiar from the standpoint of a massive barred lenticular galaxy.

1. Introduction

A galaxy's evolution is mainly influenced by its environment (Dressler 1980; Cooper et al. 2007) and stellar mass (Kauffmann et al. 2003a; Alpaslan et al. 2015). The physical mechanisms responsible for the growth of a galaxy due to the environment (galaxy nurture) include galaxy interactions, gas accretion and feedback (Kauffmann et al. 2004; van de Voort et al. 2016), ram pressure stripping (Gunn & Gott 1972), galaxy harassment (Richstone 1976; Moore et al. 1996) and halo quenching (Dekel & Birnboim 2006). On the other hand, the stellar mass affects galaxy evolution through various mechanisms such as morphological quenching (Martig et al. 2009), bar quenching (Khoperskov et al. 2018), gravitational quenching (Genzel et al. 2014), and active galactic nuclei (AGN) feedback (Croton et al. 2006). Many of these processes may act on a galaxy simultaneously throughout its lifetime, which makes it difficult to identify the effect of an individual mechanism on a galaxy, especially in the case of an over-dense environment.

A low-density environment provides a unique setting to study galaxy evolution where the environmental effects can be largely excluded. Voids are the large under-dense regions in the cosmic web having an astoundingly low mean galaxy density (Pan et al. 2012). The low-density environment of the void affects some of the properties of the void galaxies, e.g., these galaxies possess higher specific star formation rates (sSFRs) than their counterparts in the dense environment (Grogin & Geller 1999). Generally, void galaxies are star-forming low-mass systems with late-type morphology (Cruzen et al. 2002; Rojas et al. 2004; Kreckel et al. 2012; Pandey et al. 2021). A

fraction of them is found to be passive, early-type, interacting, or with active nuclei at the center (Constantin et al. 2008; Beygu et al. 2017). While a majority of the studies probing void galaxies focus on low to moderately massive void galaxies ($\lesssim 10^{10}$ $M_\odot$; see Grogin & Geller 1999; Rojas et al. 2004; Pustilnik et al. 2011; Kreckel et al. 2012), spectrophotometric properties of void galaxies falling in the higher stellar mass regime are comparatively less discussed. One of the most intuitive reasons for the underrepresentation of massive void galaxies in the literature is their sheer scarcity in the cosmic web (Grogin & Geller 1999; Tempel et al. 2011).

It is well established that the environment plays a decisive role in quenching the star formation of low-mass satellite galaxies (Bluck et al. 2020). At the same time, the situation becomes unclear in the case of high-mass central galaxies. Kauffmann et al. (2003a) have shown that the fraction of quenched galaxies increases after a threshold mass $\simeq 3 \times 10^{10}$ $M_\odot$. Agreeably various mass quenching mechanisms viz. AGN quenching, bar quenching, virial shock heating, etc., become active at high stellar masses (Zhang et al. 2021). However, these mechanisms seem to have both positive and negative evidence, e.g., Maiolino et al. (2012) reported that AGN-driven outflows at high redshifts could clear the gas out of a galaxy leading to a rapid shutdown of star formation. In contrast, the analyses done by Shangguan et al. (2018, 2020) do not support AGN feedback quenching. Therefore, the entire process of galaxy quenching is complex and demands further study.

Pandey et al. (2021) studied the properties of star-forming void galaxies based on deep ultraviolet (UV) survey in the Bootes void using the Ultraviolet Imaging Telescope (UVIT). In this work, I Zw 81 was identified as the most massive galaxy detected in the observation with strong UV emission. The galaxy is centered at $\alpha = $ 14h08m13.59 s, $\delta = $ 48d51m44.74 s, and $z = 0.052$. The main aim of our present work is to dissect the properties of I Zw 81 and understand the underlying

physical mechanisms responsible for its present state. While bright clusters and galaxy groups are expected to host galaxies of stellar masses up to $\log(M_\star/M_\odot) \gtrsim 11.70$, the void galaxies yet probed merely reach a stellar mass of $\log(M_\star/M_\odot) = 11.20$ (Penny et al. 2015). With stellar mass, $\log(M_\star/M_\odot) \approx 10.90$ (Pandey et al. 2021), I Zw 81 stands among the massive galaxies detected in isolated environments. The galaxy has been previously reported in various observational surveys of the Bootes void (Lipovetsky et al. 1988; Cruzen et al. 2002), and is known to host a Seyfert 2 AGN (Lipovetsky et al. 1988).

Few studies concentrating on the massive void galaxies $(M_\star \gtrsim 10^{10} M_\odot)$ reveal that such galaxies evolve passively and contain old stellar populations with low H_α SFRs $(<1\ M_\odot\ \text{yr}^{-1})$ and a handful of them host active nuclei (Penny et al. 2015; Fraser-McKelvie et al. 2016). These results portray that regardless of the global environment, mass quenching mechanisms active in massive galaxies are capable of shutting down ongoing star formation in a galaxy. However, the photometric properties of the galaxy in focus, I Zw 81, show blue colors on the UV and optical color–magnitude diagrams along with strong far-UV (FUV) and near-UV (NUV) emission (Pandey et al. 2021), which make the galaxy interesting to study.

Galaxies follow a strong morphology–density relation, "red and dead" galaxies with elliptical or S0 morphology, are generally found in groups and clusters, whereas "star-forming" spirals or irregular galaxies are abundant in the field environment (Dressler 1980; Peng et al. 2010b). At first, it appears that the environment is the clear driver of evolution, but a few studies state that the stellar mass correlates better with the ongoing star formation and color than the local environment density (Haines et al. 2007; Alpaslan et al. 2015), though the results are debatable (Balogh et al. 2004). It is predicted that the optical emission profile of I Zw 81 follows a De Vaucouleurs's light profile or has a large bulge surrounded by a faint disk (Cruzen et al. 1997). This structural description resonates with an early-type galaxy (ETG); thereby, I Zw 81 seems to belong to a class of massive, blue ETGs situated in a void. While blue and low-mass ETGs are reported to exist in low-to-moderate density environments, there is a dearth of similar galaxies at the high stellar mass end $(\log(M_\star/M_\odot) \sim 11.2)$. Most of the blue ETGs with stellar masses between $10^{10.5}\ M_\odot$ and $10^{11.2}\ M_\odot$ resemble major merger remnants (Kannappan et al. 2009). Through this work, we investigate if the void galaxy has undergone a similar evolution scenario.

The focus of our work is to understand the impact of mass quenching mechanisms in the absence of environmental quenching processes on the evolution of the blue and massive ETG.

The paper is organized as follows: Section 2 describes the data used in this work. In Section 3, we elaborate on our structural analysis and discuss the derived properties of I Zw 81. Section 4 summarizes SED fitting technique and derived results. Section 5 focuses on understanding the star formation activity in the galaxy. Finally, in Section 6, we discuss and conclude our findings. In this work, we assume a flat cold dark matter cosmology model with $\Omega_m = 0.27$, $\Omega_\Lambda = 0.73$, and $H_0 = 70\ \text{km s}^{-1}\ \text{Mpc}^{-1}$. A unit arcsec is equivalent to 1 kpc at $z = 0.052$.

2. Data and Observation

I Zw 81 was observed in our PILOT survey (Observing program G07-077, PI: Kanak Saha) of the Bootes void in FUV and NUV filters using UVIT onboard AstroSat. The observation was made simultaneously in UVIT F154W and N242W filters. The details of the observation and data reduction are mentioned in Pandey et al. (2021). Complementary archival imaging data of the galaxy in optical and infrared wave bands were collected from the following surveys: Sloan Digital Sky Survey Data Release 12 (SDSS DR12, Alam et al. 2015), Canada France Hawaii Telescope (CFHT, Boulade et al. 1998), Two Micron All-sky survey (2MASS, Skrutskie et al. 2006) and Wide-field Infrared Survey (WISE, Wright et al. 2010). We have also collected mid-IR 60 μm and 100 μm fluxes of the galaxy from the catalog of Moshir et al. (1990).

2.1. PSF Matching and Photometry

Each imaging survey has a specific angular resolution. The FWHM of the point-spread function (PSF) corresponding to UVIT, SDSS, and 2MASS are $\sim1\rlap{.}''5$, $1\rlap{.}''2$ and $2\rlap{.}''8$, respectively. Therefore, it is required to make the PSFs of each observation uniform prior to photometry. In our case, 2MASS has the poorest angular resolution among the above-mentioned observations. Hence, we use rescaled 2MASS PSF to homogenize UVIT and SDSS observations. We model 2MASS J-band PSF using the method described in Section 3.1 which is further rescaled to match the pixel scale of the targeted surveys (UVIT and SDSS). We create multiple PSF kernels combining rescaled J-band PSF with PSFs of FUV, NUV, and $ugriz$ wave bands. The kernels were finally used to convolve UVIT and SDSS image stamps of the galaxy. The entire process of PSF matching is carried out using the Astropy PHOTUTILS package (Bradley et al. 2020).

We perform fixed aperture photometry for all 10 bands (UVIT FUV/NUV, SDSS $ugriz$, 2MASS J/H/Ks) using a source extractor (SExtractor; Bertin & Arnouts 1996). The radius of the aperture chosen for the photometry is $\approx10''$ which is 2.5 times the optical effective radius of the galaxy (see Section 3.2). Moreover, the surface brightness profile of the 2MASS J/Ks band reaches 20/21 mag arcsec^{-2} at the same radius (Skrutskie et al. 2006). We also inspect the flux conservation of the source before and after convolution. The loss in flux due to convolution turns out to be much less than 1% within a fixed aperture. The WISE fluxes were measured within standard apertures having a radius $\sim8\rlap{.}''25$ for W1 and W2 filters and $22\rlap{.}''0$ for W3 and W4 filters (Cutri et al. 2013). The measured WISE fluxes are aperture-corrected prior to use. We apply foreground extinction corrections to fluxes in all filters using the foreground IR dust maps from Schlegel et al. (1998). Note that all the magnitudes/fluxes used are in the AB magnitude system (Oke & Gunn 1983). The magnitudes/fluxes are further converted to mJy units prior to spectral energy distribution (SED) fitting. Wherever required, K-correction in magnitudes is done using publicly available codes given by Chilingarian & Zolotukhin (2012).

3. Light Profile Decomposition

We use CFHT Megacam publicly available deep imaging data for the structural decomposition of the galaxy. The frames containing our galaxy are observed by CFHT in g- and r-wave bands for ~345 s each. These frames are well calibrated,

Table 1
GALFIT 2D Best-fit Results for the g and r Bands

Components Galfit Function	NPS PSF	Bar Sérsic				Ring Trunc. Expdisk	Inner Disk (ID) Expdisk		Outer Disk (OD) Expdisk	
Band	$(m_0)_{\rm NPS}$ (mag)	$(m_0)_{\rm bar}$ (mag)	$(r_e)_{\rm bar}$ (arcsec)	$n_{\rm bar}$	$c_{\rm bar}$	$r_{\rm break}$ (arcsec)	$(m_0)_{\rm ID}$ (mag)	$(r_s)_{\rm ID}$ (arcsec)	$(m_0)_{\rm OD}$ (mag)	$(r_s)_{\rm OD}$ (arcsec)
(1)	(2)	(3)	(4)	(5)	(6)	(7)	(8)	(9)	(10)	(11)
g	18.52	16.90	0.92	0.57	−0.32	4.20	16.36	2.04	16.53	7.35
r	17.84	16.42	0.92	0.65	−0.31	4.59	15.74	1.93	15.80	7.57
Light fraction (g band)	0.06	0.23				<0.1	0.38		0.32	

Note. Col. (2): Integrated magnitude of the nuclear point source (NPS). Col. (3)–(6): Integrated magnitude, effective radius, Sérsic index, and boxy/disky parameter of the bar. Col. (7): break radius of the ring. Col. (8)–(9): Integrated magnitude and disk scale length of the inner disk. Col. (10)–(11): Integrated magnitude and disk scale length of the outer disk. The last row represents the light fraction of all components in the CFHT g band, respectively. The magnitudes in the table are not corrected for Galactic extinction.

reduced and astrometry corrected. The CFHT observations of the galaxy (see left panel of Figure 1) suggest the presence of a ring along with a central component and a disk devoid of spiral arms.

3.1. Sky Subtraction, Masking, and PSF Modeling

We prepare cutout images centered around the galaxy from CFHT frames of size $\approx 1\rlap{.}'2$ such that $\sim$30% of the cutout contains the sky background. We run SExtractor over each CFHT cutout at a low detection threshold ($\approx$0.5) in order to generate the corresponding segmentation maps; setting a low detection threshold helps in identifying the faint features around the galaxy. These maps were used to mask the neighboring sources around the galaxy. The estimated value of sky surface brightness in g and r bands obtained using SExtractor are $\approx$25.8 mag arcsec^{-2} and 24.8 mag arcsec^{-2}, respectively. The sky background flux is subtracted from each cutout. The g- and r-band observation reaches a depth of 27.7 mag arcsec^{-2} and 27.0 mag arcsec^{-2}, respectively.

Accurate modeling of PSF holds key importance in the process of structural decomposition. We select an isolated, bright, and nonsaturated point source from CFHT g- and r-frames for PSF modeling. We use the Moffat function for modeling as it models the wings of a PSF effectively compared to a Gaussian function (Trujillo et al. 2001). The functional form of the Moffat profile used is given by:

$$f(x, y) = f_0 \left[1 + \frac{(x - x_0)^2 + (y - y_0)^2}{\alpha^2} \right]^{-\beta} \quad (1)$$

with FWHM $= 2\alpha\sqrt{2^{\frac{1}{\beta}} - 1}$. Here, f_0 is the central flux and β and α are the free parameters in the function. We model the selected point source using the 2D Moffat function present in the Astropy package. The resultant PSF FWHM in the CFHT g and r band are $0\rlap{.}''6$ and $0\rlap{.}''74$, respectively.

3.2. Structural Analysis

GALFIT is commonly used to model the light profile of a galaxy using various ellipsoidal models (Peng et al. 2002). We use GALFIT for 2D modeling of CFHT g- and r-band images of I Zw 81. The required weight (σ) images were generated internally using the value of GAIN, RDNOISE, and NCOMBINE present in the header of our input images by following

Poisson statistics. We use a combination of the following analytical profiles in our multicomponent structural modeling.

(i). *Sérsic function:* The function is one the most used function to study galaxy morphology. It is defined as follows:

$$\Sigma(r) = \Sigma_e \exp\left(-\kappa \left[\left(\frac{r}{r_e} \right)^{\frac{1}{n}} - 1 \right] \right) \quad (2)$$

where Σ_e is the surface brightness at the effective radius r_e. Here, n is the Sérsic index whose value increases as the profile of the component gets steeper in the inner part and flatter in the outskirt. The factor κ is the normalization constant dependent on n. The parameters obtained in the fit are: center coordinates, integrated magnitude (m_0), r_e, n, axis ratio (q), and position angle ($\theta_{\rm PA}$).

(ii). *Exponential disk function:* The exponential function (expdisk) is described as follows:

$$\Sigma(r) = \Sigma_0 \exp\left(-\frac{r}{r_s} \right) \quad (3)$$

where Σ_0 is the central surface brightness of the disk and r_s is the scale length of the disk. Here, the output parameters are: central coordinates, m_0, r_s, q, and $\theta_{\rm PA}$.

We run GALFIT over the g-band image with a single Sérsic function which gives a resultant $n = 5.07$ and $r_e \approx 4\rlap{.}''16$. In addition, we also obtain the central coordinates of the galaxy (x_0, y_0) from the fit. An exponential function is added in the input to fit the disk while the existing Sérsic function models the central component. The resultant output obtained by combining the two functions improves the fit but leaves a significant amount of positive fluxes in the residue. Thereafter, we added another Sérsic component and expdisk function to model the bar and outer disk, respectively. An additional parameter c is appended with the Sérsic function to model the bar to find whether the bar is disky or boxy in shape. The r_e corresponding to the Sérsic function used to model the central component successively came out to be less than the PSF FWHM which implies that the central component is small and unresolvable. Hence, we replaced the central Sérsic component with a PSF to model the component. The central coordinates of both the inner and outer disks were fixed to (x_0, y_0) while all other parameters of different components were left free

throughout the run. We also model the sky background for each runs simultaneously.

(iii). **Truncated exponential function**: We venture to model the ring using a truncated exponential disk function (Peng et al. 2010a). A truncated exponential disk function in GALFIT is primarily a hyperbolic tangential function whose functional form is as follows:

$$P(x, y) = \tanh(x, \; y; \; x_0, \; y_0, \; r_{break}, \Delta r_{soft}, q, \theta_{PA}) \quad (4)$$

where (x_0, y_0), q and θ_{PA} are the central coordinates, axis ratio, and position angle of the ring. The parameter r_{break} is the break radius at which the truncated model flux is 99% of the original untruncated model flux at that radius while Δr_{soft} is the softening length where $r_{break} \pm \Delta r_{soft}$ is the radius where the truncated model flux drops to 1% of its original flux at the same radius. The inner and outer part of the exponential disk function is modified with the same radial truncation function in our case. The free parameters in the function are: central coordinates, r_{break}, surface brightness at r_{break}, r_s, q, Δr_{soft}, θ_{PA}, etc.

To account for the observed lopsidedness of the ring, we introduce Fourier modes to the radially truncated function in order to match the actual form of the ring. The Fourier modes perturb a perfect ellipsoid as follows:

$$r(x, y) = r_0(x, y)\left(1 + \sum_{m=1}^{N} a_m \cos m(\theta + \phi_m)\right) \quad (5)$$

where $r_0(x, y)$ is the unperturbed radial coordinates, a_m is the Fourier amplitude for mode m, $\theta = \arctan((y - y_0)/(x - x_0)q)$, N is the total number of modes specified by the user and ϕ_m is the phase angle of mode m relative to θ.

We conduct subsequent reruns combining all the analytical functions discussed above, i.e., a PSF, Sérsic, two expdisk, and truncated exponential functions, until the χ_ν^2 is minimized and the residual image looks random and balanced with both negative and positive flux values. The fraction of total light recovered by our best-fit models is close to unity in each band. The χ_ν^2 values for our final fitting of CFHT g and r bands are 2.12 and 1.03, respectively. The upper panel of Figure 1 shows the CFHT g- and r-band observed images of the galaxy, best-fit models, and their corresponding residuals. The lower panel of the figure shows 1D surface brightness profiles of the galaxy, model, and its constituent components. The isophotal fittings of the model, components, and the galaxy were performed using PHOTUTILIS. Table 1 gives the details of our GALFIT output parameters for the CFHT g- and r-band models. We calculated the light fraction for each component of the galaxy in the g band using m_0 given by GALFIT. The total emission from the ring is obtained by integrating its flux contribution from the origin to r_{break}. The resultant values of the light fraction for each component are mentioned in Table 1. The choices of the chosen components for fitting are explained in Section 3.3.

3.3. Interpretation of Model Parameters

The overall light profile of the galaxy is disky with no hint of spiral arms. Hence, we categorize I Zw 81 as a lenticular galaxy. We exploit the GALFIT output parameters to briefly discuss the structural and photometric properties of all components of galaxies.

3.3.1. Nuclear Point Source, Bar, and Ring

Bulges classify into two categories, namely, classical bulges and pseudobulges (Fisher & Drory 2008; Kormendy 2016). The Sérsic index, n is a robustly used tool to differentiate bulges such that $n > 2$ for classical bulges and $n \leqslant 2$ in the case of pseudobulges. However, as the central component of I Zw 81 is modeled with a PSF function, we do not have the values of n. The fraction of light enclosed by the component is ≈ 0.06.

The bar-driven secular evolution transforms a small round classical bulge by flattening it structurally and changing it kinematically to appear like a boxy pseudobulge (Saha et al. 2012; Saha 2015). These authors have shown that a small classical bulge (bulge-to-total light ratio ~ 0.06–0.08) in Milky Way–like barred galaxies could remain hidden. I Zw 81, being barred and more massive than the Milky Way, and having a nuclear component light fraction ~ 0.06, certainly holds the possibility of a hidden small classical bulge. Neumann et al. (2017) also indicated the presence of a nuclear disk in secularly evolving galaxies. The galaxy also hosts an AGN, which may partly contribute to the observed light fraction. The overall structure of the central component remains unclear. We refer to the central component as a nuclear point source (NPS).

I Zw 81 hosts a disky bar with $r_e = 0.921$ kpc, $n \approx 0.6$, and $c < 0$. The flat intensity profile of the bar resembles those typically seen in ETGs (Williams & Evans 2017). The bar-to-total light ratio (Bar/T) is estimated to be 0.23, suggesting the presence of a strong bar (Barway & Saha 2020). Note that the incidence of a strong bar is not considered so common in S0 galaxies (Buta et al. 2010). The stellar ring is placed close to the bar end, possibly at the bar corotation resonance. The outer radius of the ring (r_{break}) is 4.2 kpc. The light emitted by the ring amounts to less than 1% of the total light inside the galaxy.

3.3.2. Inner and Outer Disks

The structural decomposition of the galactic disk in I Zw 81 reveals a "break" in its radial profile, wherein the break radius is ≈ 10 kpc (see lower panel of Figure 1). The galaxy is disk dominated as both of its disks contribute to $\approx 70\%$ of the total light in the galaxy (see Table 1). Using the integrated magnitudes in CFHT g and r bands given by GALFIT (Table 1), we estimate the central surface brightness of the inner disk (ID) and outer disk (OD) using the following Equation (6):

$$\mu_0 = m_0 + 2.5 \log(2\pi r_s^2) \quad (6)$$

The central surface brightness, $\mu_{0,ID}$ and $\mu_{0,OD}$ are further corrected for inclination and cosmological dimming effects using the following equations (Tolman 1930; Zhong et al. 2008):

$$\mu_{0,c} = \mu_0 + 2.5 \log(q) - 10 \log(1 + z). \quad (7)$$

Here, q is the axis ratio of the disk and z is the redshift of the target galaxy. We proceed to determine the central surface brightness of the disks in the B band using the following relation (Smith et al. 2002):

$$\mu_0(B) = \mu_{0,c}(g) + 0.47(\mu_{0,c}(g) - \mu_{0,c}(r)) + 0.17 \quad (8)$$

Using Equations (6), (7), and (8), the central surface brightness of the inner disk $\mu_{0,ID}(B)$ and outer disk $\mu_{0,OD}(B)$ obtained are 20.31 mag arcsec^{-2} and 23.32 mag arcsec^{-2}, respectively. The
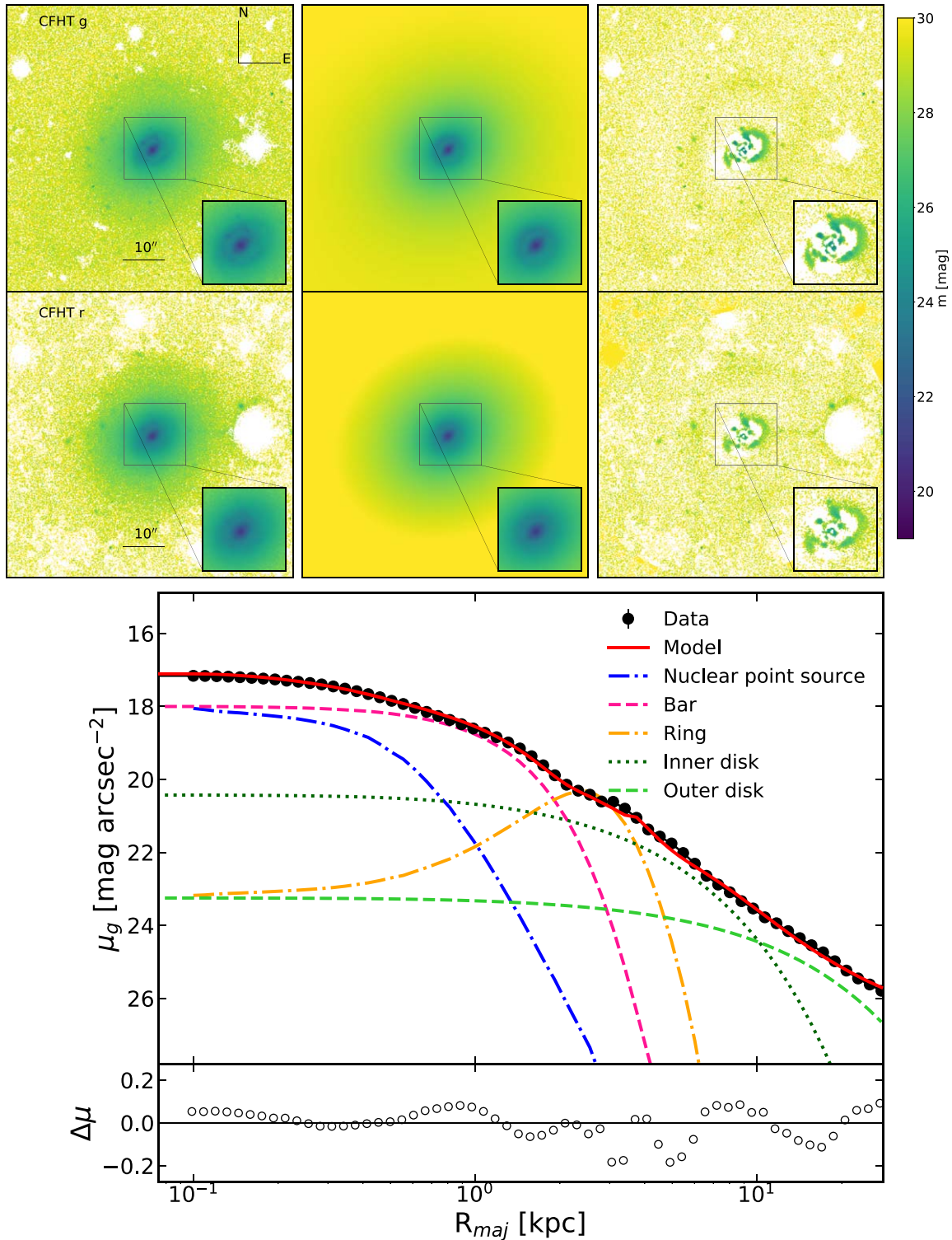
Figure 1. Upper panel) From left to right in upper (CFHT *g* band) and lower (CFHT *r* band) segments: an image of I Zw 81, GALFIT best-fit model image, and corresponding residual image in magnitude units. The inset images in all images highlight the inner region of the galaxy. (Bottom panel) Isophotal surface brightness profile of the galaxy in CFHT *g* band. Solid black circles and red line show the observed and best-fit model profiles, respectively. The surface brightness distribution of the individual component is coded with different line styles and colors, as mentioned in the legends. The residual obtained by subtracting model surface brightness from that of the galaxy is shown in the lower segment of the bottom panel.

central surface brightness, $\mu_B \geqslant 22.5$ mag arcsec^{-2}, separates low surface brightness (LSB) and high surface brightness regime (HSB; Rosenbaum et al. 2009). We conclude that the inner region or the inner disk is at HSB surrounded by an LSB outer disk.

Our structural analysis reveals that the galaxy is disk dominated with a well-defined bar and has no apparent sign of a classical bulge that could have formed due to major mergers (Kormendy 2016). Based on a suite of GALMER simulations, it is shown that in no case does a major merger S0-like remnant

form a significant stellar bar (Eliche-Moral et al. 2018). It is likely that I Zw 81 being in the void region, managed to avoid any major merger-like events during its history and evolved secularly (Kormendy & Kennicutt 2004).

4. SED Modeling and Physical Parameters

We use CIGALE (Code Investigating GALaxy Emission) for SED fitting of the galaxy to derive its physical properties such as stellar mass, SFR, dust attenuation, etc. (Boquien et al. 2019). CIGALE is a python-based approach to modeling UV to IR emission of a galaxy. It uses the Bayesian inference paradigm to determine the model parameters. The 16 wave band fluxes used by us for SED fitting are, UVIT FUV/NUV, SDSS *u/g/r/i/z*, 2MASS *J/H/Ks*, WISE W1/W2/W3/W4, and IRAS 60 μm/100 μm. The procedure used for the flux measurement in respective bands is described in Section 2.1. CIGALE offers multiple modules to model the star formation history (SFH), dust attenuation, and stellar population of a galaxy. The modules used to model each physical process are given below:

1. We select `sfh2exp` module to predict the SFH of the galaxy. The model comprises two exponentially decaying functions where the first function is used to model the long-term stellar population and the second function models the most recent starburst. Thus, the SFH model is governed by five parameters, i.e., the age of the main stellar population in the galaxy, the e-folding time of the main stellar population (τ_{main}), the e-folding time of the late starburst population (τ_{burst}), the age of the late burst population (age$_{burst}$), and the mass fraction of the late burst population (f$_{burst}$).

2. We adopt Bruzual & Charlot's (2003) library of the single stellar population to model the stellar emission of our galaxy with Salpeter's (1955) initial mass function keeping metallicity fixed at 0.02. We use the N2 method to calculate the oxygen abundance of the galaxy (Pettini & Pagel 2004).

3. We include `nebular` module to estimate the nebular emission from our galaxy. The ionization parameter (log U) is fixed at -2.5, a fraction of Lyman continuum photons escape (f$_{esc}$) and a fraction of Lyman continuum photons are absorbed (f$_{dust}$) varies between 0 and 0.1.

4. To account for the dust attenuation caused to the stellar and nebular emission, we employ `dustatt_modified_starburst` module (Calzetti et al. 2000). The value of internal reddening for nebular emission, $E(B-V)_{nebular}$, ranges between 0.37 and 0.45 in steps of 0.4. The aforementioned range encloses $E(B-V)_{nebular}$ (= 0.41) computed using the Balmer decrement method (Osterbrock & Ferland 2006). The reduction factor applied to the old stellar population varies between 0.4 and 0.6 in steps of 0.1. The attenuation curve is multiplied by a power law in wavelength, λ^{δ}, where δ varies between -0.1 and -0.5, and the amplitude of the bump at 2175 Å fixed at 3.0.

5. The dust emission process is modeled by adopting the `Dale 2014` module (Dale et al. 2014). The star-forming component in a galaxy is parameterized by a single parameter α defined as: $dM_d(U) \propto U^{-\alpha} dU$, where M_d is the dust mass, and U is the radiation field intensity. Here, α is fixed at -2.0. We include f_{AGN} to separate AGN contribution to the infrared dust emission.

6. We adopt Fritz et al.'s (2006) AGN template in our SED fitting to model AGN emission. The module deals with

Table 2
CIGALE SED Fitting Parameters

| Parameters	Values
Star formation history - `sfh2exp`	
τ_{main} (Myr)	3000, 5000, 7000, **9000**, 10000
age (Myr)	**8000**, 9000, 10000, 11000, 12000
τ_{burst} (Myr)	50 , **100**, 500, 1000, 2500, 5000
burst$_{age}$ (Myr)	**500**, 1000, 1500, 2000
f_{burst}	0.01, **0.1**, 0.25, 0.50
`nebular`	
f_{esc}	**0.0**, 0.1
f_{dust}	**0.0**, 0.1
Dust attenuation - `dustatt_modified_starburst`	
$E(B-V)_{nebular}$	0.37, **0.41**, 0.45
$E(B-V)_{factor}$	0.4, **0.5**, 0.6
powerlaw_slope	-0.1, **-0.3**, -0.5
Dust emission - `Dale 2014`	
f_{AGN}	**0.0**, 0.1
AGN - Fritz et al. (2006)	
r_ratio	30, 60, **100**
β	-0.75, **-0.25**
γ	2.0, **4.0**, 6.0
opening_angle	60, 100, **140**
psy	30.1, **70.1**
fracAGN	**0.0**, 0.1, 0.2

Note. The best-fit parameters are in boldface.

seven free parameters: r is the ratio of maximum to minimum radii of the dust torus, β and γ describe the dust density with respect to the radius and opening angle (θ), ψ is the angle between the AGN axis and the line of sight and fracAGN is the ratio between AGN IR luminosity to total IR luminosity.

Table 2 comprises all the selected modules and input parameters. The best-fit parameters are in boldface. The combined grid parameters yield 139,96,800 model templates. The best-fit SED model is shown in Figure 2.

The best-fit value of fracAGN is 0.0, which implies that the obtained SED is compatible with no AGN contribution to the total IR emission. We set the value of fracAGN to 0.1 (the next admissible value) and compute the model SED and various physical parameters. The values of χ^2_{ν} at fracAGN = 0.0 and 0.1 are 0.5 and 1.5, respectively. We show the best-fit model SEDs corresponding fracAGN = 0./0.1 in Figure 2. The physical properties of I Zw 81 show slight variation in either case, suggesting that both values are equally likely to model the broadband emission of the galaxy. However, the best-fit value of the parameter never exceeds 0.1. Hence, we suspect the presence of a low-luminosity AGN (Ciesla et al. 2018).

The stellar mass of the galaxy obtained from our SED fitting is $\sim 7.8 \times 10^{10} M_{\odot}$. The age of the main stellar population is 8 Gyr, and the mass ratio of young-to-old stars is ≈ 0.001, implying the presence of a dominant fraction of old and evolved stars in the galaxy. We compare the properties of I Zw 81 with a sample of bright S0 galaxies from Barway et al. (2013). The stellar population age of the bright S0 galaxies is more than 9 Gyr, whereas $D_n(4000)$ index (Balogh et al. 1999) for the sample peaks at 2.0 and GALEX NUV$-$r color for such
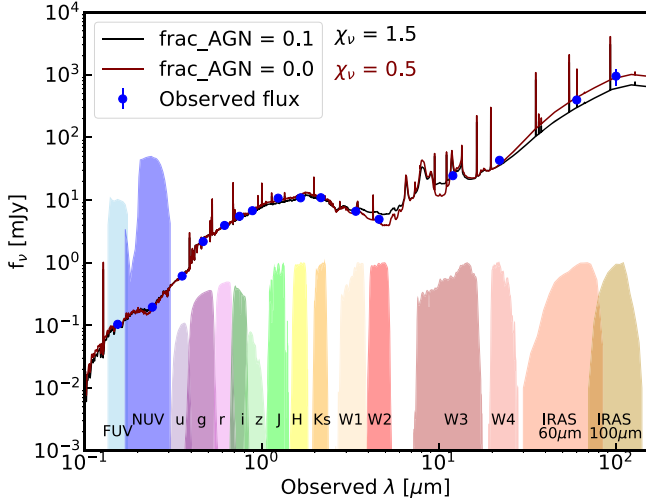
Figure 2. Best-fit SEDs (fracAGN = 0./0.1) of I Zw 81 produced by CIGALE. The input broadband fluxes are marked with blue circles. The best-fit parameters can be found in Table 2. The error bars on the measured fluxes denote 1σ error bar. The filter response curves are shown in the figure with different colors.

galaxies is dominantly greater than 5.4 mag. These galaxies are generally present in groups and clusters. In the case of I Zw 81, the NUV − r color is 3.35 mag (GALEX NUV − r = 3.46 mag) and $D_n(4000) = 1.57$. These parameters suggest that I Zw 81 is more star-forming, and the stellar population age of the galaxy is lower than the bright S0 galaxies studied by Barway et al. (2013).

Using SFR and $M_\star$ obtained from SED fitting, we construct the sSFR versus $M_\star$ diagram for the galaxy as shown in Figure 3. The background galaxies, showing bimodal distribution are taken from Salim et al. (2016). The void galaxies with $M_\star > 5 \times 10^{10}\ M_\odot$ present in the figure are from Pan et al. (2012). We procure the values of SED-generated sSFRs and $M_\star$ of these void galaxies from the Galaxy and Mass Assembly DR2 catalog (Liske et al. 2015). Figure 3 shows that a majority of massive void galaxies evolve passively while a small fraction of them, including I Zw 81 lie in the star-forming region. Our analysis confirms that the massive I Zw 81 is star forming and hosts a younger stellar population than its counterparts in groups and clusters.

5. Central Star Formation and the Blue Bar

Figure 3 shows that the sSFR of I Zw 81 lie nearly half a dex above the star-forming main sequence. We inspect if such vigorous star formation activity is global or localized to certain regions in the galaxy with the help of CFHT observation and GALFIT model parameters. Figure 4 depicts the (g−r) color map of I Zw 81 wherein the outer radii of the stellar ring and the bar within r_e are shown. The bar appears to be optically blue while there is an asymmetry in the color of the disk inclining toward the redder side of the color scale.

We use the integrated magnitudes provided in Table 1 to find the colors of individual components and qualitatively consider them as a proxy for the stellar population age. The observed optical colors $(g−r)_{bar}$, $(g−r)_{ID}$, and $(g−r)_{OD}$ are 0.44 mag, 0.58 mag, and 0.69 mag, respectively. It turns out that the bar is the bluest, and the outer LSB disk is the reddest in our galaxy like the case of Malin 1 whose central region has an S0 morphology with a bluer bar (Saha et al. 2021). Based on

optical colors, we argue that I Zw 81 contains a mix of old and young stars, wherein the old stellar population dominates as the bulk of emission from the galaxy originates from the disks. A similar observation where disks of barred galaxies were redder than the unbarred galaxies is also reported by Kruk et al. (2018). The work suggests that the secular evolution of galaxies driven by the bar generally leads to such a scenario.

The bluer bar in the central region is associated with a radially asymmetric star-forming ring with an average (g−r) color = 0.45 mag (Figure 4). Very few similar star-forming rings in S0 galaxies have been reported recently (Proshina et al. 2019; Sil'chenko & Moiseev 2020). What is more intriguing is the presence of two bluer optical clumps on the ring. It is not clear how these S0 galaxies get their cold gas to drive the star formation, or could it be residual star formation activity or the UV upturn seen in some Ellipticals (O'Connell 1999; Kaviraj et al. 2007).

The UV morphology of the central region of the galaxy is insightful. Figure 5 displays strong FUV and NUV emissions (observed by UVIT) from the galaxy. The FUV emission in a galaxy arises from the photosphere of young O- and B-type stars, and traces star formation up to ∼100 Myr (Kennicutt & Evans 2012). Alternatively, UV emission could arise from evolved stellar populations such as main-sequence turnoff or extreme horizontal branch stars (O'Connell 1999). However, the broadband UV and UV-optical colors of the galaxy are bluer, e.g., FUV−NUV, FUV−r, and NUV−r are ≈0.66 mag, 4.15 mag, and 3.35 mag, respectively (Pandey et al. 2021), which do not seem to satisfy the UV upturn criteria (Kaviraj et al. 2007; Yi et al. 2011). The broadband SED (Figure 2) does not illustrate any signature of the classic UV upturn case as shown by the sample presented in Yi et al. (2011).

5.1. Star Formation in Clumps

As seen in Figure 5, the surface brightness of the centermost region of I Zw 81 (equivalent to aperture, $r = 1.5''$; enclosing the bar) in FUV and NUV observation are ∼23 mag arcsec^{-2} and ∼22 mag arcsec^{-2}, respectively. The FUV surface brightness level at the end of the ring ($r \simeq 4.25$ kpc) is about 25 mag arcsec^{-2}. Beyond the extent of the outer stellar ring, the FUV emission declines sharply. Apart from the central bright UV blob, the ring at the end of the bar hosts two star-forming UV clumps (marked as C1 and C2 in Figure 5). These clumps were identifiable in the UV and optical color map of the galaxy. In a Hα imaging survey, Weistrop et al. (1995) pointed out two small emission regions in I Zw 81, in a direction coinciding with the positions of the UV clumps. In order to measure the FUV SFR of the clumps, we first run SExtractor on the CFHT g-band image to find their central coordinates. Thereafter, we measure FUV flux around the central coordinates within a circular aperture of radius $1''$ and subtract the background emission from the galaxy to get the net FUV within each clump. We calculate the FUV SFR of the clumps using the following equation (Kennicutt 1998):

$$SFR = 1.4 \times 10^{-28} L_{FUV} (\text{erg s}^{-1}\ \text{Hz}^{-1}), \tag{9}$$

The resultant internal extinction corrected FUV SFRs for clumps C1 and C2 are 0.13 $M_\odot \text{yr}^{-1}$ and 0.23 $M_\odot \text{yr}^{-1}$, respectively. The detection of these clumps in Hα imaging and the estimated values of FUV SFRs are a testimonial of vigorous star formation activity in clumps and not the case of UV upturn. The evidence shown above using the UV emission and optical
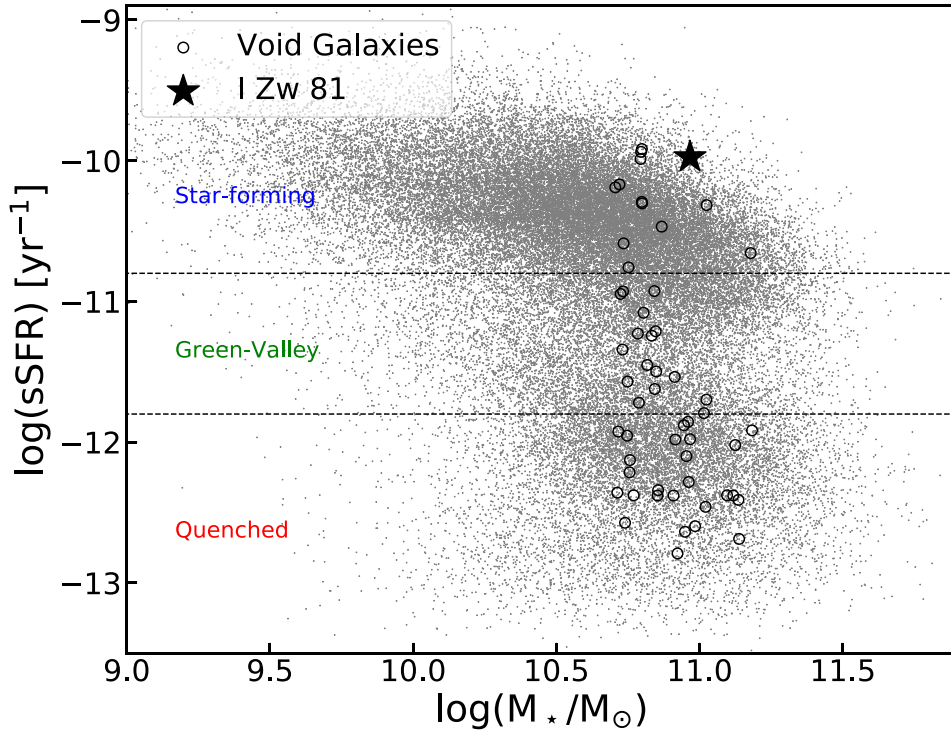
Figure 3. $M_\star$ vs. sSFR distribution for void galaxies. The black star marker denotes IZw81. Black open circles are void galaxies with $M_\star > 5 \times 10^{10}\ M_\odot$ (Pan et al. 2012). The background galaxies (gray dots) are taken from Salim et al. (2016). The figure is divided into three sections: star-forming region (log sSFR $\geqslant -10.8$), green valley region ($-10.8 > $ log sSFR > -11.8), and quenched region (log sSFR $\leqslant -11.8$; Barway & Saha 2020).

colors is sufficient to claim that the entire central region (4−5 kpc) enclosing the bar is star forming.

To investigate whether the star-forming barred S0 galaxies are common in our local environment (z < 0.1), we selected a sample of S0 (S0/a and S0) galaxies from Nair & Abraham (2010). The catalog subcategorizes galaxies based on their nuclear activity and marks galaxies with bars. We created a subset of S0 galaxies showing bar-like features (weak, intermediate, strong, nuclear, lens). The values of $M_\star$ and SED SFRs for the sample were taken from Salim et al. (2016) catalog. Figure 6 shows $M_\star$ versus sSFR distribution for all (barred /barred Seyfert 2) S0 galaxies alongside I Zw 81. We notice that the frequency of star-forming barred S0 galaxies shows a gradual decrease with increasing stellar mass, and all star-forming AGN-active barred S0 galaxies are less massive than I Zw 81.

6. Discussion

We used multiwavelength imaging data to perform 2D structural decomposition and modeled the SED of the galaxy to understand the present evolutionary state of I Zw 81. The disk-dominated lenticular galaxy turns out to be star forming with stellar mass $\log(M_\star/M_\odot) = 10.9$. The photometric properties shown by I Zw 81 are intriguing, e.g., shallow positive color gradient, star-forming ring, and central star formation in an old stellar population-dominated massive galaxy. Several external and internal conditions could lead to the observed state of the galaxy, e.g., minor mergers drive about half of the star formation activity in the local Universe (Kaviraj 2014) which may account for the star formation in I Zw 81. Moreover, two internal features identified in the galaxy, i.e., AGN (with marginal evidence) and bar, are also known to affect the SFR in

massive central disk galaxies similar to I Zw 81 (Zhang et al. 2021). We discuss the impact of these processes on the galaxy.

6.1. Possibility of a Minor Merger Interaction?

One of the mechanisms responsible for observing a blue bar in S0 galaxies could be tidal torque and minor mergers (Barway & Saha 2020). These mechanisms were envisaged to explain the sudden bar rejuvenation seen in several S0 galaxies present in the intermediate-density environment.

Based on the NED, WISEA J140811.38+485344.2, present at a distance of 0.12 Mpc, is the nearest neighbor to the galaxy. The stellar mass of WISEA J140811.38+485344.2 is ∼1/11 times I Zw 81 (Pandey et al. 2021). Considering this as an ongoing interaction between the galaxies, it is viable that it could excite a bar in the host. However, the weak interaction seems insufficient to explain the observed star formation. Thereby, we inspect CFHT observations and GALFIT residues of the galaxy (Figure 1) to look for any sign of minor merger remnants in its morphology. The completeness limit of CFHT g-band observation = 23.7 mag which is roughly 1.5 mag deeper than standard SDSS images (magnitude limit = 22.2 mag in g band; York et al. 2000). In fact, the depth of our CFHT observation (Section 3.1) is comparable to deep SDSS Stripe 82 images used by Kaviraj (2014) to identify the minor mergers in local galaxies. We find a tidal tail-like feature in the observation marked by a crescent shape segment and horizontal and vertical boxes in the left panel of Figure 7. The surface brightness within the vertical and horizontal boxes is 26.2 mag arcsec^{-2} and 25.8 mag arcsec^{-2}, respectively. Although SDSS observation (right panel of Figure 7) does not reveal any such features, the incidence of (previous) minor merger can not be ruled out based on the CFHT data. The interactions might have
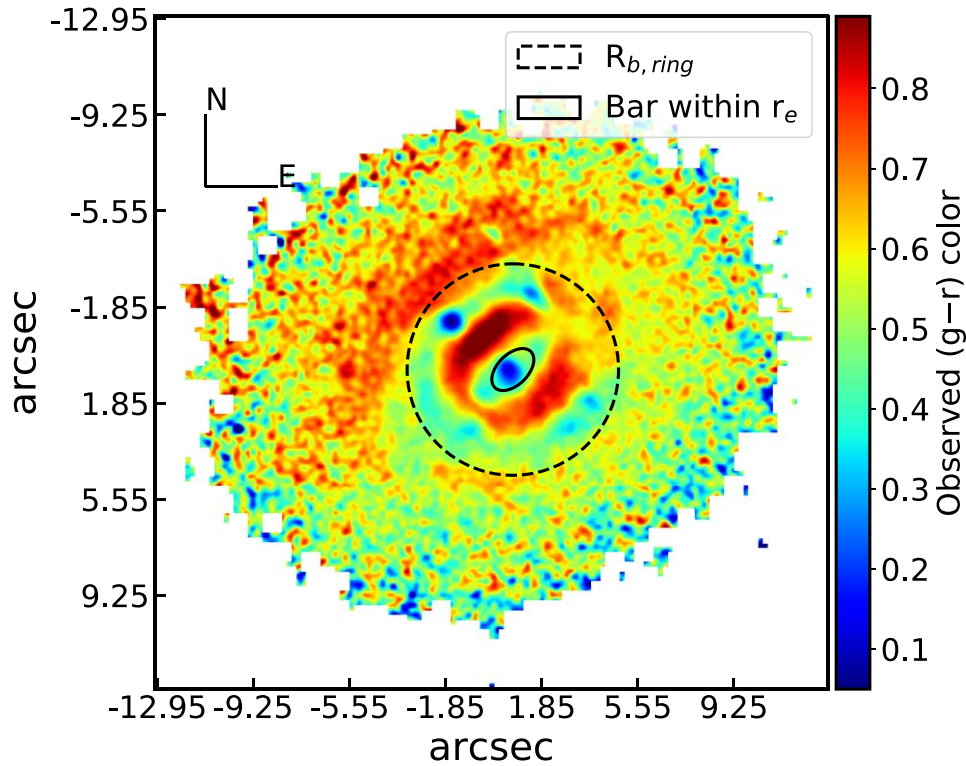
Figure 4. CFHT $g-r$ color map of I Zw 81. The colors shown are not corrected for Galactic or internal extinction. The black solid ellipse traces the GALFIT modeled bar ($r_e = 0\rlap{.}{''}92$, $\theta_{P.A.} = 45°$ $q = 0.55$) whereas the radius of the black dotted circle denotes $r_{break}(= 4\rlap{.}{''}2)$.

elevated the ongoing star formation activity in the galaxy. However, Kaviraj (2014) stated that minor mergers do not significantly enhance the SFR of ETGs compared to late-type galaxies due to their low internal gas content. We need further investigation for a strong inference.

6.1.1. Effect of Interaction on the Bar

The size of bars strongly correlates with the stellar mass of galaxies which grows in size and strength with time (Erwin 2019). As a result, a massive ETG like I Zw 81 is expected to host a large bar. Instead, the detected bar is surprisingly small, with a substantial Bar/T ratio. A weak tidal interaction with the neighboring galaxy may excite the bar (Peschken & Łokas 2019) but does not justify the observed gas influx in the bar. We argue that the small blue bar is an outcome of minor merger interactions with satellite galaxies. The young bar could be tidally induced due to recent gas accretion. Interestingly, the small bar with high SFR fits in the result presented by Fraser-McKelvie et al. (2020) where the scaled bar length of the galaxy correlates with its offset from the star-forming main sequence.

### 6.2. Role of AGN in Central Star Formation

AGNs tend to affect the evolution of galaxies in multiple ways. They spew cold gas out of the interstellar medium of the galaxy and prevent the gas from cooling down, thus leading to star formation suppression (i.e., negative feedback; Fabian 2012). On the other hand, AGN activity could also compress the cold and dense gas in the galaxy, which may enhance the ongoing SFR (i.e., positive feedback; Silk 2013).

Mid-IR colors are suitable for understanding the properties of active nuclei as the UV-optical radiation from the accretion

disk of the AGN is absorbed by the dusty torus and reradiated in mid-IR wave bands. The mid-IR colors for I Zw 81 are W1–W2 = 0.3 mag (Vega) and W2–W3 = 2.9 mag (Vega). The colors infer a little reradiated mid-IR flux from the accretion disk of the galaxy (Stern et al. 2012). The result agrees with our SED analysis, where the AGN is recognized to have low luminosity. Shao et al. (2010) have reported that the star formation in the hosts of low-luminosity AGNs is similar to non-AGN massive galaxies. Such hosts have an old stellar population similar to a normal ETGs ($D_n > 1.7$; Kauffmann et al. 2003b), but I Zw 81 possesses a younger stellar population and star formation extends further up to the outer boundary of the ring (4–5 kpc). Evidently, the low-luminosity AGN is insufficient in quenching the ongoing central star formation.

6.3. Role of Bars in Central Star Formation

Bars are known to regulate the flow of gas to the galactic center and enhance star formation activity, which in turn leads to the growth of central mass concentration in galaxies (Wang et al. 2012). However, there is no clear picture of the morphology of star formation sites in the bar region, as many bars are devoid of star formation due to the sweeping of gas material by the bar itself (Khoperskov et al. 2018). Some studies found that the inner rings of barred galaxies hinder the passage of cold gas toward the galactic center by redirecting the gas in the resonant rings (Neumann et al. 2019; Fraser-McKelvie et al. 2020). Massive gas-poor lenticular galaxies show FUV emission only in the central region of the bar, which is due to bar quenching of the disks (Díaz-García et al. 2020). However, the FUV emission in I Zw 81 is spread throughout the bar despite having a stellar ring (see Figure 5). It is highlighted that only gas-rich late-type galaxies exhibit star
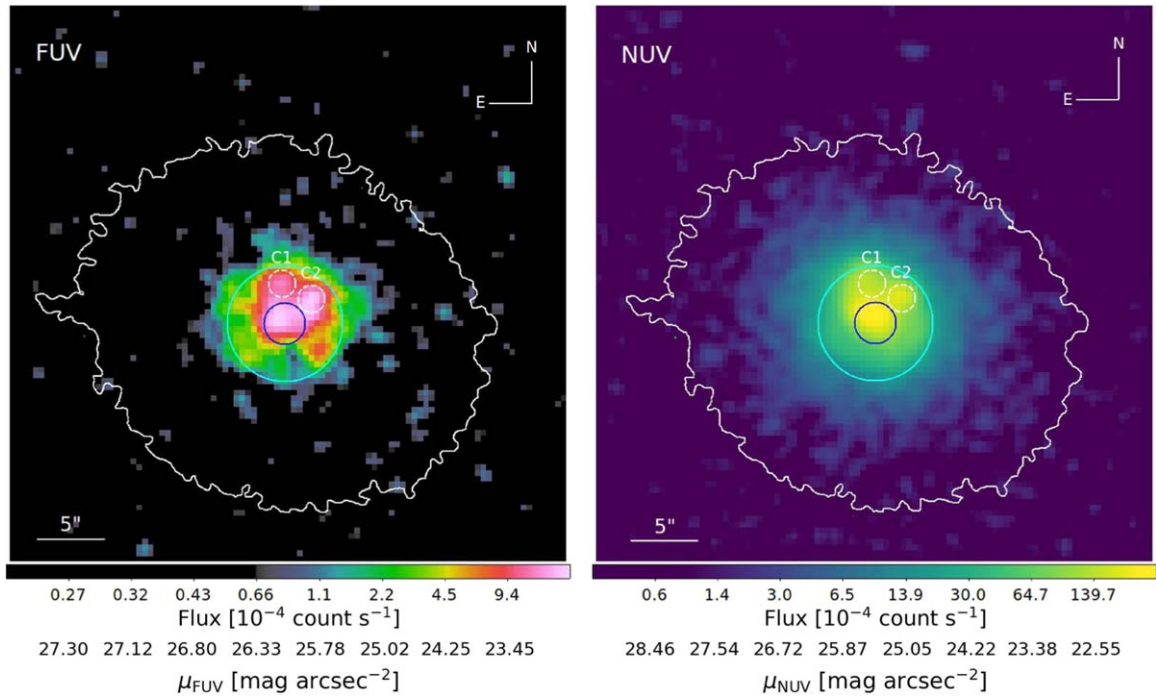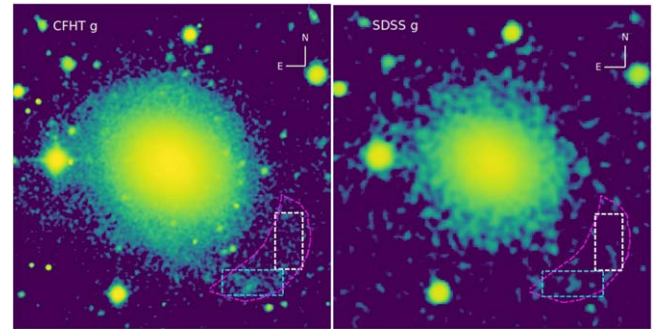
Figure 5. UVIT, FUV, and NUV images of the galaxy in the left and right panels, respectively. The color bar represents the flux and surface brightness distribution on the image. The 3σ limiting surface brightness values for FUV and NUV observation are 27.37 mag arcsec^{-2} and 27.92 mag arcsec^{-2}, respectively. White contour represents the boundary of the galaxy seen in the optical wave band, whereas blue and cyan colored circles show the central region of the galaxy ($r = 1.5''$) and the outer radius of the ring ($r = 4.2''$). The star-forming clumps C1 and C2 are enclosed in a white open circle of radius $1''$ each.
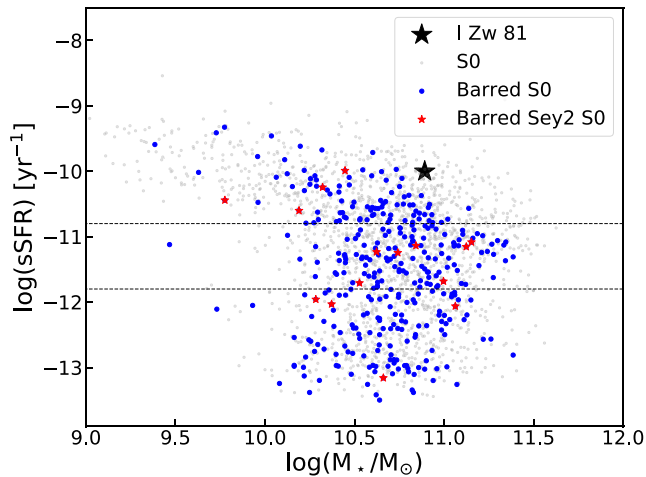
Figure 6. $M_\star$ vs. sSFR distribution for a sample of S0, barred S0, and barred Sy2 S0 galaxies. The S0 sample is taken from Nair & Abraham (2010).

Figure 7. A comparison between CFHT and SDSS g-band images of I Zw 81. The magenta-colored crescent segment, vertical, and horizontal boxes highlight the tidal tail-like feature identified in CFHT observation. The same regions are overlayed on SDSS g-band image.

formation along the bar (Díaz-García et al. 2020) as shown by I Zw 81.

Since the bar is a strong nonaxisymmetric pattern in a galaxy, it can produce enough torque to efficiently transport cold gas from the outskirts to the inner region (Kormendy & Kennicutt 2004), excite strong star formation activity (Fanali et al. 2015) as well as triggers nuclear activity (Smethurst et al. 2021). However, this picture of gas inflow becomes deceptive or rather ill understood in the case of I Zw 81. The entire disk region in the galaxy is devoid of any spiral structure that facilitates the gas flow from the outskirts to the inner region, from where the bar torque would be more active (Saha & Jog 2014).

I Zw 81 is one of the few star-forming barred S0 galaxies with an active nucleus in the sample shown in Figure 6. The result highlights the peculiarity of the galaxy. The galaxy seems to be sufficiently gas rich compared to other massive barred lenticular galaxies shown in Figure 6 to support the ongoing star formation. Apart from the recent gas inflow due to a minor merger, the sparse environment of the void may aid the present state of I Zw 81. Void galaxies tend to conserve their gas supplies for an extended time period due to the lack of environmental quenching processes. The combined effect perhaps leads to sSFR enhancement in the galaxy. The observed central star formation is a result of the funneling of gas to the galactic center by the bar. A detailed study of gas kinematics is essential to precisely understand the state of I Zw 81.

7. Summary and Conclusion

We study the structural and star formation properties of a massive lenticular void galaxy—I Zw 81. Our assimilated results are peculiar for a massive barred S0 galaxy in a void. We briefly summarize our results as follows.

1. The galaxy has a complex morphological structure. It comprises an NPS, a bar, a distorted ring, an HSB inner disk, and an LSB outer disk.
2. Our SED analysis shows that the sSFR of the galaxy lies half a dex above the star-forming main sequence. This ongoing star formation is only limited to the central region of the galaxy.
3. The bar and inner ring display bluer optical colors compared to the disks.
4. We detect a discernible FUV emission from the central region ($4-5$ kpc) of the galaxy. The FUV emission in I Zw 81 is comparatively more widespread than typically seen in gas-poor S0 galaxies. The incidence of FUV emission along the bar requires the host galaxy to be gas rich.
5. We find a signature of tidal interaction in the galaxy using CFHT observation. We argue that the observed SFR is due to minor merger interactions and a lack of galaxy nurture in a void. The young bar driving the gas toward the galactic center could be tidally induced due to the interaction.
6. The low-luminosity AGN is shown to be insufficient in quenching the central star formation.

Software: astropy (Astropy Collaboration et al. 2018), CIGALE (Boquien et al. 2019), Source Extractor (Bertin & Arnouts 1996), GALFIT(Peng et al. 2010a).

ORCID iDs

Divya Pandey https://orcid.org/0000-0002-4656-056X
Kanak Saha https://orcid.org/0000-0002-8768-9298
Ananta C. Pradhan https://orcid.org/0000-0001-5808-0654

References

Alam, S., Albareti, F. D., Allende Prieto, C., et al. 2015, ApJS, 219, 12
Alpaslan, M., Driver, S., Robotham, A. S. G., et al. 2015, MNRAS, 451, 3249
Astropy Collaboration, Price-Whelan, A. M., Sipőcz, B. M., et al. 2018, AJ, 156, 123
Balogh, M. L., Baldry, I. K., Nichol, R., et al. 2004, ApJL, 615, L101
Balogh, M. L., Morris, S. L., Yee, H. K. C., Carlberg, R. G., & Ellingson, E. 1999, ApJ, 527, 54
Barway, S., & Saha, K. 2020, MNRAS, 495, 4548
Barway, S., Wadadekar, Y., Vaghmare, K., & Kembhavi, A. K. 2013, MNRAS, 432, 430
Bertin, E., & Arnouts, S. 1996, A&AS, 117, 393
Beygu, B., Peletier, R. F., van der Hulst, J. M., et al. 2017, MNRAS, 464, 666
Bluck, A. F. L., Maiolino, R., Piotrowska, J. M., et al. 2020, MNRAS, 499, 230
Boquien, M., Burgarella, D., Roehlly, Y., et al. 2019, A&A, 622, A103
Boulade, O., Vigroux, L. G., Charlot, X., et al. 1998, Proc. SPIE, 3355, 614
Bradley, L., Sipőcz, B., Robitaille, T., et al. 2020, astropy/photutils: v1.0.0 Zenodo
Bruzual, G., & Charlot, S. 2003, MNRAS, 344, 1000
Buta, R., Laurikainen, E., Salo, H., & Knapen, J. H. 2010, ApJ, 721, 259
Calzetti, D., Armus, L., Bohlin, R. C., et al. 2000, ApJ, 533, 682
Chilingarian, I. V., & Zolotukhin, I. Y. 2012, MNRAS, 419, 1727
Ciesla, L., Elbaz, D., Schreiber, C., Daddi, E., & Wang, T. 2018, A&A, 615, A61
Constantin, A., Hoyle, F., & Vogeley, M. S. 2008, ApJ, 673, 715
Cooper, M. C., Newman, J. A., Coil, A. L., et al. 2007, MNRAS, 376, 1445
Croton, D. J., Springel, V., White, S. D. M., et al. 2006, MNRAS, 365, 11
Cruzen, S., Wehr, T., Weistrop, D., Angione, R. J., & Hoopes, C. 2002, AJ, 123, 142
Cruzen, S. T., Weistrop, D., & Hoopes, C. G. 1997, AJ, 113, 1983
Cutri, R. M., Wright, E. L., Conrow, T., et al. 2013, Explanatory Supplement to the AllWISE Data Release Products, Explanatory Supplement to the AllWISE Data Release Products
Dale, D. A., Helou, G., Magdis, G. E., et al. 2014, ApJ, 784, 83
Dekel, A., & Birnboim, Y. 2006, MNRAS, 368, 2
Díaz-García, S., Moyano, F. D., Comerón, S., et al. 2020, A&A, 644, A38
Dressler, A. 1980, ApJ, 236, 351
Eliche-Moral, M. C., Rodríguez-Pérez, C., Borlaff, A., Querejeta, M., & Tapia, T. 2018, A&A, 617, A113
Erwin, P. 2019, MNRAS, 489, 3553
Fabian, A. C. 2012, ARA&A, 50, 455
Fanali, R., Dotti, M., Fiacconi, D., & Haardt, F. 2015, MNRAS, 454, 3641
Fisher, D. B., & Drory, N. 2008, AJ, 136, 773
Fraser-McKelvie, A., Pimbblet, K. A., Penny, S. J., & Brown, M. J. I. 2016, MNRAS, 459, 754
Fraser-McKelvie, A., Aragón-Salamanca, A., Merrifield, M., et al. 2020, MNRAS, 495, 4158
Fritz, J., Franceschini, A., & Hatziminaoglou, E. 2006, MNRAS, 366, 767
Genzel, R., Förster Schreiber, N. M., Lang, P., et al. 2014, ApJ, 785, 75
Grogin, N. A., & Geller, M. J. 1999, AJ, 118, 2561
Gunn, J. E., & Gott, J. R. I. 1972, ApJ, 176, 1
Haines, C. P., Gargiulo, A., La Barbera, F., et al. 2007, MNRAS, 381, 7
Kannappan, S. J., Guie, J. M., & Baker, A. J. 2009, AJ, 138, 579
Kauffmann, G., White, S. D. M., Heckman, T. M., et al. 2004, MNRAS, 353, 713
Kauffmann, G., Heckman, T. M., White, S. D. M., et al. 2003a, MNRAS, 341, 54
Kauffmann, G., Heckman, T. M., Tremonti, C., et al. 2003b, MNRAS, 346, 1055
Kaviraj, S. 2014, MNRAS, 440, 2944
Kaviraj, S., Schawinski, K., Devriendt, J. E. G., et al. 2007, ApJS, 173, 619
Kennicutt, R. C. J. 1998, ARA&A, 36, 189
Kennicutt, R. C., & Evans, N. J. 2012, ARA&A, 50, 531
Khoperskov, S., Haywood, M., Di Matteo, P., Lehnert, M. D., & Combes, F. 2018, A&A, 609, A60
Kormendy, J. 2016, in Galactic Bulges, ed. E. Laurikainen, R. Peletier, & D. Gadotti (Berlin: Springer), 431
Kormendy, J., & Kennicutt, R. C. J. 2004, ARA&A, 42, 603
Kreckel, K., Platen, E., Aragón-Calvo, M. A., et al. 2012, AJ, 144, 16
Kruk, S. J., Lintott, C. J., Bamford, S. P., et al. 2018, MNRAS, 473, 4731
Lipovetsky, V. A., Neizvestny, S. I., & Neizvestnaya, O. M. 1988, Soobshcheniya Spetsial'noj Astrofizicheskoj Observatorii, 55, 5
Liske, J., Baldry, I. K., Driver, S. P., et al. 2015, MNRAS, 452, 2087
Maiolino, R., Gallerani, S., Neri, R., et al. 2012, MNRAS, 425, L66
Martig, M., Bournaud, F., Teyssier, R., & Dekel, A. 2009, ApJ, 707, 250
Moore, B., Katz, N., Lake, G., Dressler, A., & Oemler, A. 1996, Natur, 379, 613
Moshir, M., Kopan, G., Conrow, T., et al. 1990, BAAS, Vol. 22, 1325
Nair, P. B., & Abraham, R. G. 2010, ApJS, 186, 427
Neumann, J., Wisotzki, L., Choudhury, O. S., et al. 2017, A&A, 604, A30
Neumann, J., Gadotti, D. A., Wisotzki, L., et al. 2019, A&A, 627, A26
O'Connell, R. W. 1999, ARA&A, 37, 603
Oke, J. B., & Gunn, J. E. 1983, ApJ, 266, 713
Osterbrock, D. E., & Ferland, G. J. 2006, Astrophysics of Gaseous Nebulae and Active Galactic Nuclei (Sausalito, CA: University Science Books)
Pan, D. C., Vogeley, M. S., Hoyle, F., Choi, Y.-Y., & Park, C. 2012, MNRAS, 421, 926
Pandey, D., Saha, K., & Pradhan, A. C. 2021, ApJ, 919, 101
Peng, C. Y., Ho, L. C., Impey, C. D., & Rix, H.-W. 2002, AJ, 124, 266
Peng, C. Y., Ho, L. C., Impey, C. D., & Rix, H.-W. 2010a, AJ, 139, 2097

Peng, Y.-j., Lilly, S. J., Kovač, K., et al. 2010b, ApJ, 721, 193
Penny, S. J., Brown, M. J. I., Pimbblet, K. A., et al. 2015, MNRAS, 453, 3519
Peschken, N., & Łokas, E. L. 2019, MNRAS, 483, 2721
Pettini, M., & Pagel, B. E. J. 2004, MNRAS, 348, L59
Proshina, I. S., Kniazev, A. Y., & Sil'chenko, O. K. 2019, AJ, 158, 5
Pustilnik, S. A., Tepliakova, A. L., & Kniazev, A. Y. 2011, AstBu, 66, 255
Richstone, D. O. 1976, ApJ, 204, 642
Rojas, R. R., Vogeley, M. S., Hoyle, F., & Brinkmann, J. 2004, ApJ, 617, 50
Rosenbaum, S. D., Krusch, E., Bomans, D. J., & Dettmar, R. J. 2009, A&A, 504, 807
Saha, K. 2015, ApJL, 806, L29
Saha, K., Dhiwar, S., Barway, S., Narayan, C., & Tandon, S. 2021, JApA, 42, 59
Saha, K., & Jog, C. J. 2014, MNRAS, 444, 352
Saha, K., Martinez-Valpuesta, I., & Gerhard, O. 2012, MNRAS, 421, 333
Salim, S., Lee, J. C., Janowiecki, S., et al. 2016, ApJS, 227, 2
Salpeter, E. E. 1955, ApJ, 121, 161
Schlegel, D. J., Finkbeiner, D. P., & Davis, M. 1998, ApJ, 500, 525
Shangguan, J., Ho, L. C., Bauer, F. E., Wang, R., & Treister, E. 2020, ApJS, 247, 15
Shangguan, J., Ho, L. C., & Xie, Y. 2018, ApJ, 854, 158
Shao, L., Lutz, D., Nordon, R., et al. 2010, A&A, 518, L26
Sil'chenko, O., & Moiseev, A. 2020, A&A, 638, L10
Silk, J. 2013, ApJ, 772, 112
Skrutskie, M. F., Cutri, R. M., Stiening, R., et al. 2006, AJ, 131, 1163
Smethurst, R. J., Simmons, B. D., Coil, A., et al. 2021, MNRAS, 507, 3985
Smith, J. A., Tucker, D. L., Kent, S., et al. 2002, AJ, 123, 2121
Stern, D., Assef, R. J., Benford, D. J., et al. 2012, ApJ, 753, 30
Tempel, E., Saar, E., Liivamägi, L. J., et al. 2011, A&A, 529, A53
Tolman, R. C. 1930, PNAS, 16, 511
Trujillo, I., Aguerri, J. A. L., Cepa, J., & Gutiérrez, C. M. 2001, MNRAS, 328, 977
van de Voort, F., Bahé, Y. M., Bower, R. G., et al. 2016, MNRAS, 466, 3460
Wang, J., Kauffmann, G., Overzier, R., et al. 2012, MNRAS, 423, 3486
Weistrop, D., Hintzen, P., Liu, C., et al. 1995, AJ, 109, 981
Williams, A. A., & Evans, N. W. 2017, MNRAS, 469, 4414
Wright, E. L., Eisenhardt, P. R. M., Mainzer, A. K., et al. 2010, AJ, 140, 1868
Yi, S. K., Lee, J., Sheen, Y.-K., et al. 2011, ApJS, 195, 22
York, D. G., Adelman, J., Anderson, J. E. J., et al. 2000, AJ, 120, 1579
Zhang, C., Peng, Y., Ho, L. C., et al. 2021, ApJ, 911, 57
Zhong, G. H., Liang, Y. C., Liu, F. S., et al. 2008, MNRAS, 391, 986